Journal of Applied Polymer Science

Mesoporous Silica Particles Grafted with Polystyrene Brushes as a Nucleation Agent for Polystyrene Supercritical Carbon Dioxide Foaming

Jintao Yang, Lingqi Huang, Yuefang Zhang, Feng Chen, Mingqiang Zhong
College of Chemical Engineering and Materials Science, Zhejiang University of Technology, Hangzhou 310014, People's Republic of China
Correspondence to: M. Zhong (E-mail: zhongmingqiang@hotmail.com)

ABSTRACT: In this study, spherical ordered mesoporous silica (s-OMS) was applied as a new type of nucleating agent in polystyrene (PS) foaming with supercritical CO_2 as a blowing agent. These s-OMS particles were modified by the selective grafting of PS brushes on the outside surface, by which the mesoporous structure inside particles could be maintained. Transmission electron microscopy, X-ray diffraction, thermogravimetric analysis, Fourier transform infrared spectroscopy, and Brunauer–Emmett–Teller surface area analysis were used to characterize the structure of the original and modified particles; these indicated that the PS brushes were grafted on the outside surface and the inside porous structure were maintained. PS/s-OMS–PS composites were prepared by a solution blending method, and the s-OMS–PS particles could have been well dispersed in the PS matrix because of the surface modification. Subsequently, PS and composite microcellular foams were prepared by a batch foaming process, and the morphology characterization on these foams showed that the s-OMS particles exhibited an excellent heterogeneous effect on PS foaming. The heterogeneous effect became more significant when the foaming temperature or saturation pressure was low. © 2013 Wiley Periodicals, Inc. J. Appl. Polym. Sci. 130: 4308–4317, 2013

KEYWORDS: foams; grafting; polystyrene; ordered mesoporous silica; carbon dioxide

Received 4 February 2013; accepted 11 May 2013; Published online 17 July 2013
DOI: 10.1002/app.39532

INTRODUCTION

Over the decades, polymeric foams have been studied extensively in the academic community and widely applied in industry because of their superior characteristics, including their light weight, high strength-to-density ratio, and high thermal insulation.[1] Polymeric foams are generally prepared by a blowing agent, which can expand the materials' applicability in some specific area. Blowing agents can be chemical agents or physical ones, and a lot of polymer processing methods, such as extrusion and injection molding, can be adopted.[2] According to the cell morphology, polymeric foams are divided into different categories: open-celled foams, close-celled foams, microcellular foams, and nanofoams. *Microcellular foams* are defined as foams in which the cell diameter is less than 10 μm and the cell density is higher than 10^9 cell/cm^3. This type of foam exhibits much better mechanical properties, fatigue resistance, and other properties compared with polymers without foaming and general foams.[3–5] The mechanical properties of microcellular foams depend highly on the cell structure. Generally, for a given bulk density, a smaller cell diameter and higher cell density always results in a higher mechanical performance.[6] Therefore, one of the important desires for microcellular foams is the preparation of foams with a small cell size and high cell density; thus, ultramicrocellular foams and nanofoams are proposed. Another issue in this field is the use of supercritical carbon dioxide ($scCO_2$) to produce the microcellular foams because of its environmental affinity. However, it is hard because $scCO_2$ has a high diffusivity and moderate solubility in most polymers. In a foaming process, cells are formed by the following steps: cell nucleation, cell growth, and cell coalescence. Among these steps, nucleation is one of the most important steps determining the cell diameter and cell density. On the basis of this issue, the addition of nanoparticles may supply a solution for producing microcellular foams in an easy way because the nanoparticles have a high specific surface area and offer more nucleation sites than traditional nucleating agents.[7] In the past, various fillers, including SiO_2,[8–10] clay,[11] graphite oxide,[12] carbon nanotubes, and carbon fiber,[13] have been applied to produce microcellular foams with a smaller size and uniform cell structure. These studies have demonstrated that the nucleation effect is related to the shape, size, surface properties, and dispersion state of these nanoparticles.[14] In general, nanoparticles with small sizes and uniform dispersions always produce more heterogeneous nucleation sites and, hence, more bubbles in the sample. In addition, the surface

© 2013 Wiley Periodicals, Inc.

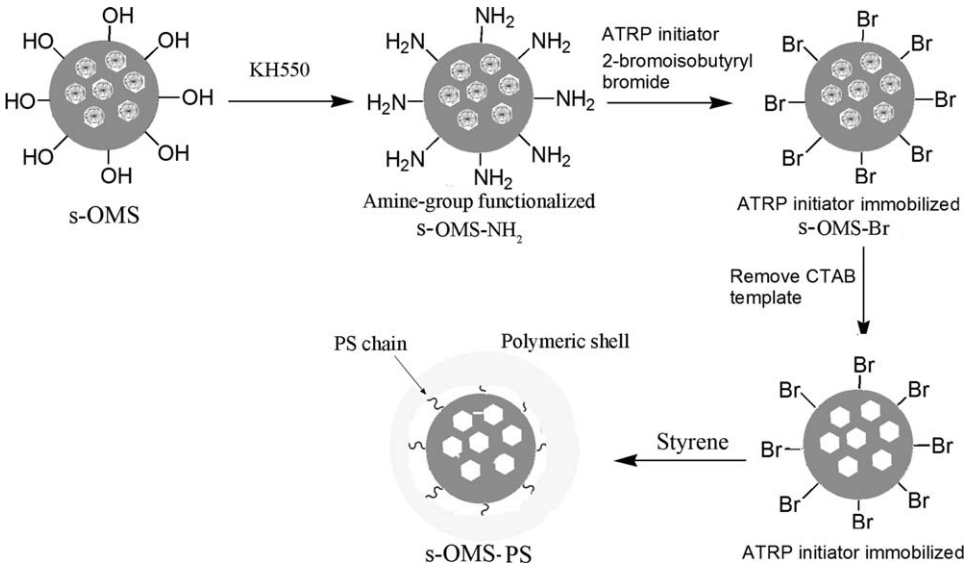

Figure 1. Schematic of the surface modification of the s-OMS particles.

properties of the nanoparticles result in various contact angles between the polymer, CO_2, and nanoparticles, which also greatly affect the nucleating performance. To evaluate the nucleating performance of nanoparticles, the nucleation efficiency, which is represented by the ratio of heterogeneous sites and the number of nanoparticles, was proposed.[15] When evaluated with this indicator, however, the heterogeneous nucleating performance of most nanoparticles is very poor. Therefore, it is critical to prepare nucleation agents with a high efficiency and to understand how to manipulate the nucleation performance and cell morphology.

Ordered mesoporous silica (OMS) is a form of newly developed silica that possesses a numerous ordered mesoporous structure. Because of this unique structure, it has attracted a great deal of interest and has been widely applied in the fields of catalysis, separation, sensors, drug delivery, and optical devices.[16–19] Among these applications, CO_2 adsorption materials are of importance because they have significant values for both the industrial and academic communities. OMS has numerous mesopores and a high specific area, offering a high space for CO_2 adsorption. When the pore channels are amine-functionalized, an even higher CO_2 adsorption capacity can be obtained.[20] In this study, we proposed the use of OMS as a heterogeneous nucleating agent in polymer foaming by $scCO_2$. To verify this idea, spherical ordered mesoporous silica (s-OMS) particles with a diameter of around 200 nm were prepared. It is well known that in the study of heterogeneous nucleation effect of inorganic particles, the dispersion state of these particles in the polymer matrix must be taken into consideration. To solve the dispersion problem, a layer of polystyrene (PS) brushes was introduced onto the outside surface of the s-OMS particles to increase their compatibility with PS. At the same time, the mesoporous structure was maintained by a selective initiator supporting technique. The maintained pore channels were designed as reservoirs for $scCO_2$, that is, the blowing agent. The morphology and heterogeneous nucleation effect of these morphologically controlled s-OMS particles were investigated. The results reported herein indicate that the OMS materials had the potential to be used as efficient nucleating agents for polymer foaming.

EXPERIMENTAL

Materials

Hexadecyl trimethyl ammonium bromide (CTAB) was purchased from Jingchun Reagent Co., Ltd. (Shanghai, China). Styrene was purchased from Lingfeng Chemical Reagent Co., Ltd. (Shanghai, China), and was distilled under reduced pressure to remove the inhibitor before use. Tetraethoxysiliane, 3-triethoxysilylpropylamine (APTES; 98%), 2-bromoisobutyryl bromide, *N,N,N′,N″,N″*-pentamethyl diethylenetriamine (PMDETA; 98%), and copper(I) bromide (CuBr; analytical reagent, purified before use) were purchased from Aladdin Reagent(Shanghai) Co., Ltd., and were used as received. CO_2 was purchased from Jingong Gas Co., Ltd. (Hangzhou, China). Other chemical agents were commercial products with chemical purity and were used as received.

Sample Preparation

Synthesis of the s-OMS Particles. A typical synthesis procedure by a sol–gel method was performed as follows: 1.00 g of CTAB and 0.32 g of NaOH were dissolved in 500 mL of deionized water with vigorous stirring to form a clear solution. Then, 20 mL of tetraethoxysiliane was slowly added drop by drop under stirring, whereupon a white precipitate appeared. The suspension was stirred at 80°C for 6 h, and the product was collected by centrifugation, washed with deionized water, and dried in air to get the s-OMS particles with a template agent.

s-OMS Particles Selectively Grafted with Atom Transfer Radical Polymerization (ATRP) Initiators. The surface modification of the prepared s-OMS particles are shown in Figure 1. To prepare the s-OMS grafted with ATRP initiator, 1.0 g of s-OMS

particles were dispersed in anhydrous toluene by ultrasound; then, an excess mount of APTES (2.9 mL) was added to the solution. The reaction between APTES and hydroxyl on silica was conducted for 24 h at the reflux temperature of toluene. The particles modified by APTES (s-OMS–NH_2) were recovered by centrifugation/acetone washing cycles and dried at 50°C overnight. The immobilization of the ATRP initiator was realized by the reaction between 2-bromoisobutyryl bromide and s-OMS–NH_2. s-OMS–NH_2 (1.0 g) was mixed with 200 mL of anhydrous dichloromethane in a round-bottle flask, and 10 mL of triethylamine and 15 mL of 2-bromoisobutyryl bromide were dropped in slowly. The reaction was carried out in an ice–water bath for 2 h after ultrasonic treatment, and this was continued for 24 h at 20°C. The product was centrifuged, washed with toluene and acetone, and dried *in vacuo*. To remove the template inside the particles, the particles were extracted by the refluxing of a hydrochloric acid/methanol mixture (1.0 mol/L) at 100°C for 24 h. After the extraction, the modified OMS materials were achieved after drying and were marked as s-OMS–Br.

Surface-Initiated ATRP of Styrene on the Modified OMS Materials. s-OMS–Br (0.40 g) was dispersed in 10 mL of styrene by an ultrasonic method in a Schlenk flask equipped with a magnetic stirring bar and N_2 inlet. The polymerization was carried out with the following steps. The mixture was degassed by three freeze–pump–thaw cycles. In the unfrozen state, CuBr and PMDETA (molar ratio of the initiating sites of s-OMS–Br/CuBr/PMDETA = 1:1:2) were added under the protection of an N_2 flow. The flask was then subjected to two additional freeze–pump–thaw cycles and then immersed in an oil bath heated to 120°C. Stirring was started immediately after thawing. After 24 h, the flask was exposed to air to terminate the polymerization. The solid product was dissolved in tetrahydrofuran (THF). The particles were isolated by centrifugation at 8000 rpm, then dispersed in THF, and centrifuged again. This purification cycle was repeated four times to remove the adsorbed polymers, and the product (s-OMS–PS) was dried in a vacuum oven at 80°C for 24 h.

Preparation of the Composites. The obtained s-OMS–PS was first well dispersed in THF after ultrasonic treatment; PS pellets were then added and stirred until complete dissolution. Subsequently, the suspension was poured into a large excess of cold methanol to precipitate the polymers. The solid obtained by filtration was dried in a vacuum oven at 80°C for 24 h. Finally, the dried powder samples were shaped into plates by compression with hydraulic presses (Labtech Engineering Company, Ltd.) operated at 200°C (both upboard and downboard). A similar shaped pure PS plate was also prepared in the same manner for comparison.

Preparation of the Composite Microcellular Foams. Batch foaming of the PS and composites was conducted in a high-pressure chamber with $scCO_2$ as the blowing agent. The plate samples were placed in the chamber and then saturated by $scCO_2$ at 13.8 MPa and 120°C for 18 h. The pressure in the chamber was monitored and adjusted by an ISCO D-series pump. The samples were foamed by the rapid release of the pressure in 0.5 s and the fixing of the foam morphology by cooling with an ice–water mixture.

Characterization

The morphologies of the original and modified s-OMS particles were observed by transmission electron microscopy (TEM) with a Philips FEI microscope (Tecnai G2 F30 S-Twin, FEI Co., The Netherlands) at an acceleration voltage of 300 kV. The samples for TEM observations were prepared by the placement of 10 μL of solution of the particles in ethanol and THF on copper grids.

X-ray diffraction (XRD) patterns were recorded on an X'Pert PRO instrument (PANalytical) with Cu Kα radiation. The powders were placed on a bracket sample holder. The data were recorded with a scanning rate of 1°/min and a scanning scope between 1 and 10°.

Nitrogen adsorption/desorption isotherms were measured at −196°C with a Micromeritics ASAP 2020 analyzer. Before the measurements, the samples were degassed *in vacuo* at 150°C for at least 6 h. The Brunauer–Emmett–Teller (BET) method was used to calculate the specific surface areas, and the pore size distributions were derived from the Barrett–Joyner–Halenda (BJH) model.

Fourier transform infrared (FTIR) spectra were recorded on a Nicolet 6700 instrument. Samples were prepared by the compression of the powder with KBr.

The glass-transition temperatures (T_g's) of the particles grafted with PS brushes and the composites were measured by differential scanning calorimetry (DSC; TA-Q100). The samples were heated from 40 to 180°C at a heating rate of 20°C/min under an N_2 flow of 10 mL/min.

Thermogravimetric analysis (TGA) was carried out on an SDT Q600 instrument (Thermal Analysis Instruments) at a heating rate of 20°C/min in the range from room temperature to 700°C under a nitrogen atmosphere.

The morphology of the PS/s-OMS composites was examined with a transmission electron microscope (JEM-1200EX, Japan Electron Optics Laboratory, Tokyo, Japan) at an acceleration voltage of 80 kV. Ultrathin slices (<100 nm thickness) for observation were cut from the plate samples.

The morphology of the foams was observed with a scanning electron microscope (Hitachi S-4700, Japan). The foamed samples were cryofractured in liquid nitrogen, and the fracture surface was sputter-coated with gold. The cell size and cell density [N_c; estimated by eq. (1)] were calculated via image analysis:

$$N_c = \frac{6V_f}{\pi D^3} \tag{1}$$

where D is the cell-average diameter obtained from scanning electron microscopy (SEM) images and V_f is the void fraction of the foamed sample. The void fraction is defined as

$$V_f = 1 - \frac{\rho_f}{\rho} \tag{2}$$

where ρ_f is the bulk foam density measured according to ASTM D 792 and ρ is the density of the unfoamed material.

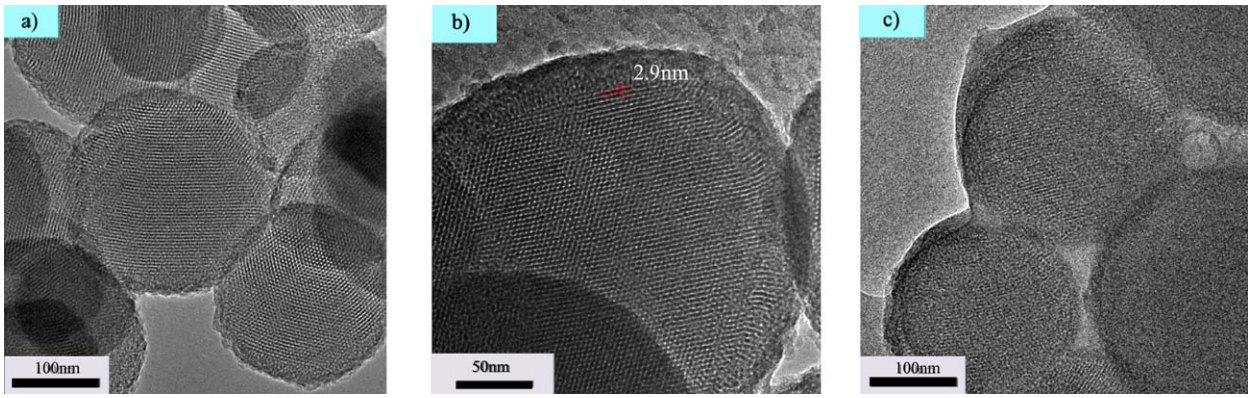

Figure 2. TEM images of (a) s-OMS, (b) s-OMS with higher magnification, and (c) s-OMS–PS. [Color figure can be viewed in the online issue, which is available at wileyonlinelibrary.com.]

RESULTS AND DISCUSSION

Preparation of the s-OMS Particles and Their Surface Modification

Figure 2(a) shows typical TEM images of the synthesized s-OMS particles, from which the morphologies and the internal pore structure of these particles could be observed. It was clear that the samples were monodispersed spheres with an average diameter of around 200 nm. The grid morphology inside these spheres indicated that a lot of mesopores were contained. As estimated from the TEM observations [as shown in Figure 2(b)], the average pore size was about 2.9 nm; this agreed well with the pore size value characterizing MCM-41 type mesoporous materials.[21] The spherical OMS particles were then modified by the grafting of the PS brushes on the outside surface. Herein, before template removal, amination modification and ATRP initiator immobilization were conducted on the OMS particles. In this case, the ATRP initiator was selectively grafted onto the outside surface. By surface-initiated ATRP, the PS brushes were grafted on the particle surface. Figure 2(c) shows the morphologies of the particles with PS brushes. As shown in the figure, the s-OMS particles were covered with a layer of PS brushes to form a core–shell structural complex. At the same time, the pores inside the particles were well retained. The N_2 adsorption–desorption isotherm and the corresponding BJH pore size distribution curves of the s-OMS particles are shown in Figure 3. The nitrogen adsorption–desorption isotherm of these particles gave a representative type-IV isotherm, in which an adsorption/desorption hysteresis loop at P/P_0 = 0.25–0.5 (where P_0 is the saturated vapor pressure of nitrogen at −195°C, and P is the real pressure of nitrogen) was observed; this indicated the presence of a mesoporous framework. From the pore size distribution curve, a narrow-pore distribution centered at 3.4 nm was observed. The BET specific surface area, pore volume, and pore diameter of the silica spheres are summarized in Table I, which shows that BET surface area and pore volume of the s-OMS particle were about 691.7 m^2/g and 0.85 cm^3/g, respectively. Figure 4 shows the XRD pattern of the prepared s-OMS particles. Three peaks at 2θ values of 2.1, 3.6, and 4.2° and corresponding to the crystal faces (100), (110), and (200), respectively, were detected. These peaks indicated a long-range order with a hexagonal pore structure.[22] The XRD patterns of the modified s-OMS are also shown in Figure 4. Compared with the original s-OMS, the intensity of the XRD peaks of the modified sample was much lower. This decrease in the

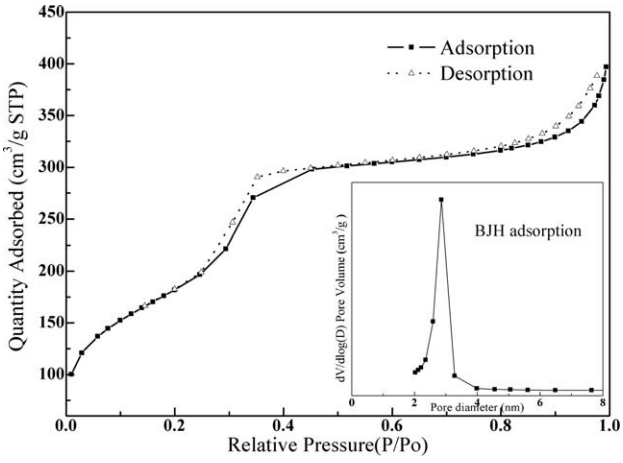

Figure 3. N_2 adsorption/desorption isotherms of s-OMS and the pore distribution curve (inserted). V = pore volume; D = hole diameter of cylindrical calculated from pore volume.

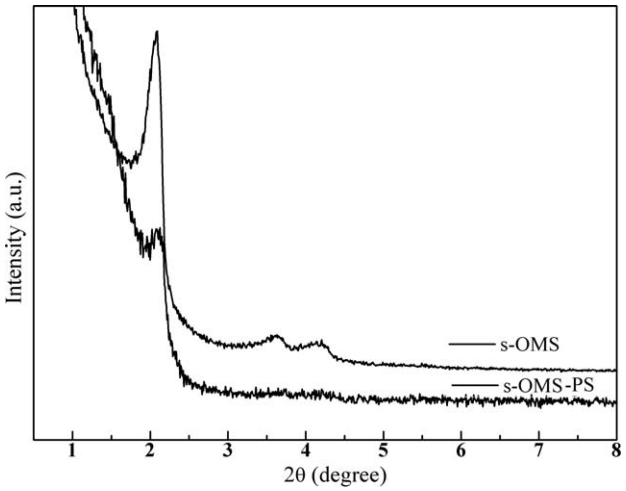

Figure 4. Small angle X-ray patterns of the bare OMS and s-OMS–PS.

Applied Polymer SCIENCE

Table I. Structural Properties of the Synthesized s-OMS

Sample	BET specific surface area (m^2/g)[a]	Pore volume (cm^3/g)	Pore diameter (nm)[b]	Pore diameter (nm)[c]
OMS	691.76	0.85	3.38	3.47

[a] Single-point specific surface area.
[b] Calculated by the BJH method; desorption.
[c] Calculated by the BJH method; adsorption.

intensity of the XRD peaks may have been due to the disorderliness caused by the PS brushes.

To illustrate the composition of the original and modified s-OMS particles, FTIR spectroscopy was applied to the analysis of the functional groups on these samples. Figure 5 shows the FTIR spectra of the original s-OMS, s-OMS grafted with initiator, and s-OMS grafted with PS brushes. In these spectra, the strong peaks at 1080 and 1635 cm^{-1} were assigned to the stretching vibrations of Si—O and the effect of hydroxyls outside of OMS, respectively, which were characteristic of the s-OMS samples. For the s-OMS samples modified by the initiator, two small peaks at 2920 and 2850 cm^{-1}, corresponding to C—H stretching and bending vibrations, were detected. This result indicates the successful grafting of the initiator. In the case of s-OMS grafted with the PS brushes, the peaks at 2920 and 2850 cm^{-1} became much stronger than those of s-OMS with initiator; this indicated that many more organics were attached. Furthermore, some new peaks characterizing the benzene ring, such as peaks at 3029 cm^{-1} from the aromatic carbon–hydrogen bond and at 1603 cm^{-1} corresponding to C—C aromatic ring stretching, were observed. These peaks supplied further evidence proving that the s-OMS were successfully modified by grafted PS brushes.

TGA was used to further confirm the grafting of the PS brushes and their loading on the s-OMS particles. The weight loss values as a function of the temperatures of the original and modified s-OMS particles are shown in Figure 6. The weight loss of

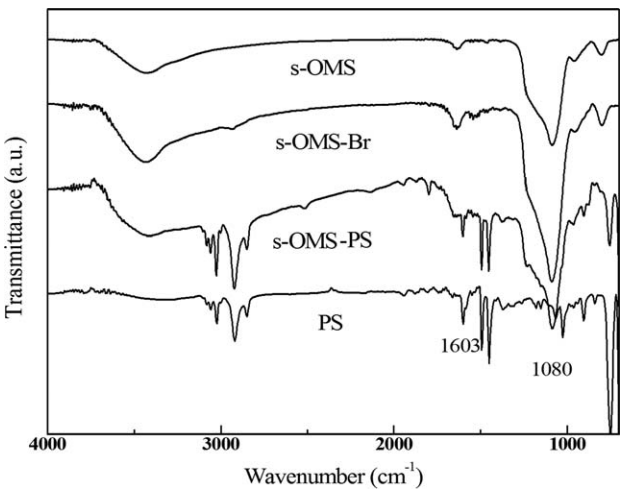

Figure 5. FTIR spectra of (a) s-OMS, (b) s-OMS–Br, (c) s-OMS–PS, and (d) PS.

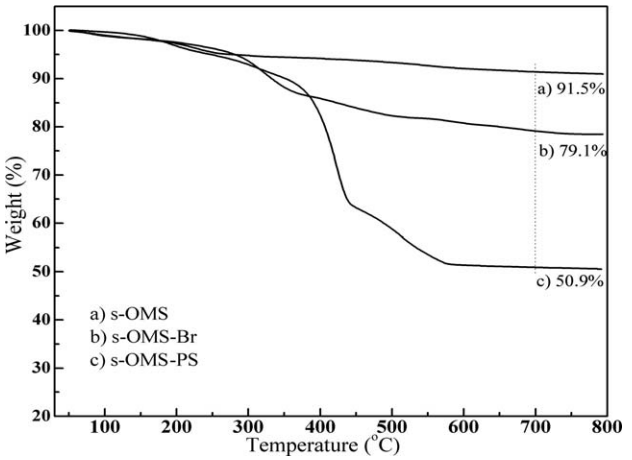

Figure 6. TGA curves of (a) s-OMS, (b) s-OMS–Br, and (c) s-OMS–PS.

pristine s-OMS particles from ambient temperature to 700°C was around 8.5 wt %; this was mainly caused by the loss of adsorbed water on the surface of the particles and inside of the pores. When the initiator was grafted onto the surface of the particles, the weight loss mainly occurred between 250 and 450°C. The total weight loss was around 20.9 wt % and was due to the decomposition of the grafted initiators. For the s-OMS grafted with the PS brushes, the weight loss between 250 and 450°C became much more significant, and a weight loss of around 49.1 wt % was observed that was mainly caused by the macromolecules. From eq. (3), the graft ratio of organics was calculated to be about 0.87 g/g of s-OMS:

$$g = \frac{1 - w_{s-OMS-PS}}{w_{s-OMS-PS}} - \frac{1 - w_{s-OMS}}{w_{s-OMS}} \quad (3)$$

where g is the graft ratio and $w_{s\text{-}OMS\text{–}PS}$ and $w_{s\text{-}OMS}$ are the weights of the respective samples at 700°C.

Preparation, Properties, and Foaming of the PS/s-OMS Composites

PS/s-OMS composites with different s-OMS loadings were prepared by a solution blending method.[9] Figure 7 gives the typical TEM images of the composites, indicating the structure and dispersion state of the s-OMS particles in the PS matrix. It was clear that the grafted PS brushes increased the compatibility between the s-OMS particles and PS matrix, and thus, the modified particles could be uniformly dispersed. Most particles were individually dispersed, and some were dispersed as aggregates with several particles. From the image with high magnification, the morphology of the particles could be observed. The PS brush layer on the particle surface and pore inside the particles was obvious and indicated that the blending process did not destroy the porous structure.

The thermal properties of the composites were evaluated by DSC measurements from which the glass-transition of the composites could be obtained, and the results are shown in Figure 8. PS had a T_g of around 98°C. When the s-OMS particles were introduced, this value increased. The composite with 0.5 wt % s-OMS silica showed a T_g of around 108°C. To illustrate the effect of s-OMS on the T_g of PS, the T_g of the PS brushes on

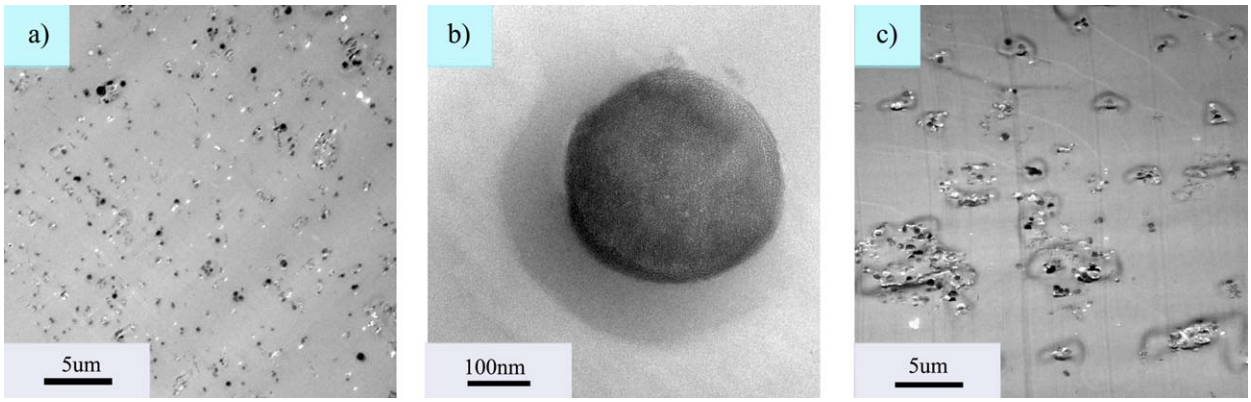

Figure 7. TEM images of composites with 5.0 wt % of particles: (a) PS/s-OMS–PS, (b) PS/s-OMS–PS with higher magnification, and (c) PS/s-OMS. [Color figure can be viewed in the online issue, which is available at wileyonlinelibrary.com.]

the surface of s-OMS particles was also measured. Because of the strong confinement effect of s-OMS, the PS brushes showed an even higher T_g. In the composites, the PS brushes entangled with the molecular chains of the PS matrix, and this led to the decreased mobility of the chain segments. So, a high temperature was needed for the chain segmental movements, and thus, a high T_g was observed for the composite.

For the foaming process of the polymer with $scCO_2$ as the blowing agent, the solubility of $scCO_2$ was one of the key factors affecting the foam morphologies. One of the initial purposes of this study was to use the porous structure and high specific area of the s-OMS particles to enhance the $scCO_2$ solubility in the composite. Before the foaming process, we measured the solubility of $scCO_2$ in pure PS and PS/s-OMS by a gravimetric method, in which the samples were saturated by CO_2 at 10.0 MPa at 35.0°C and then rapidly taken out from the vessel for weighing. The mass losses of the samples with time were recorded, as shown in the curves in Figure 9. The good linear relationship between the mass uptake and the square root of desorption time indicated that the diffusion of CO_2 obeyed Fick's law in these samples. The slope of the desorption line reflected the diffusion of $scCO_2$ in the polymer and/or composites. As shown in Figure 9, the desorption lines for the composites were more sloppy than those of pure PS; this indicated that $scCO_2$ had a higher diffusively in the composites. We postulate that some $scCO_2$ was stored in the pores of the s-OMS particles, and this part of $scCO_2$ was easily dissipated. Moreover, the interface between the s-OMS particles and PS matrix might have also induced the high dissipation of $scCO_2$ from the composites. Through the fitting and extrapolation of the curves, the initial solubility represented by the intercept of fitting lines in both the pure polymer and composites was obtained. The initial solubility of CO_2 in the pure PS was around 10.25 wt %. For the composites containing 3 and 5 wt % s-OMS particles, the CO_2 solubilities were about 10.53 and 10.33 wt %, respectively, almost similar to that in pure PS. In our previous study, the $scCO_2$ solubility was decreased by the addition solid silica particles because these particles occupied some volume but did not have $scCO_2$ adsorption capacity. However, the s-OMS particles possessed a lot of pores and a high specific area, and the pores made the particles become excellent reservoirs for $scCO_2$. The storage of $scCO_2$ inside the s-OMS particles compensated for the loss of $scCO_2$ solubility caused by the volume occupation of silica in the composites.

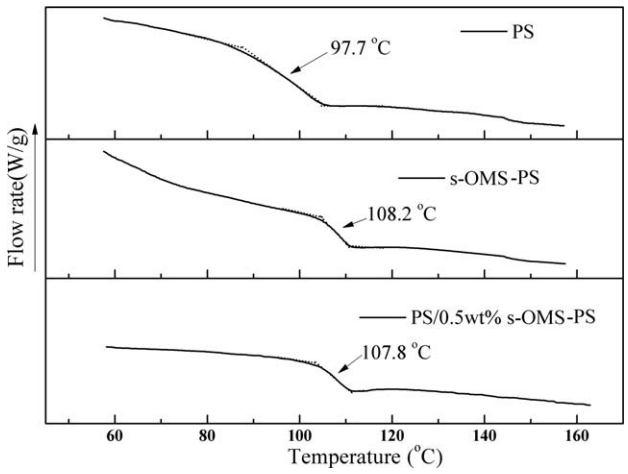

Figure 8. DSC curves of the PS, s-OMS–PS, and composite with 0.5 wt % s-OMS particles.

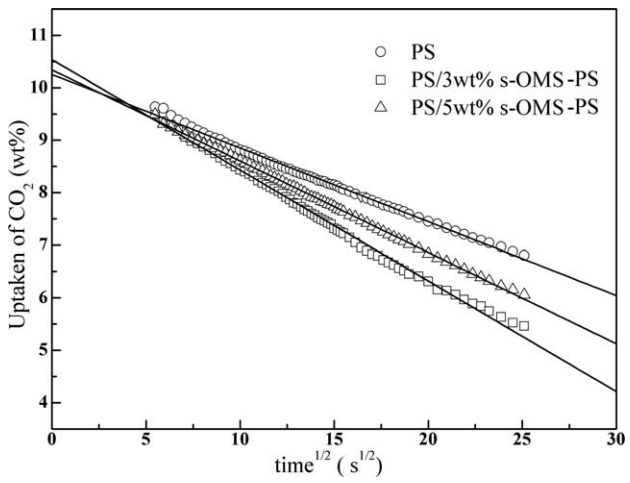

Figure 9. Desorption curves of the PS and composite with saturation conditions under 10 MPa and 35°C.

Applied Polymer SCIENCE

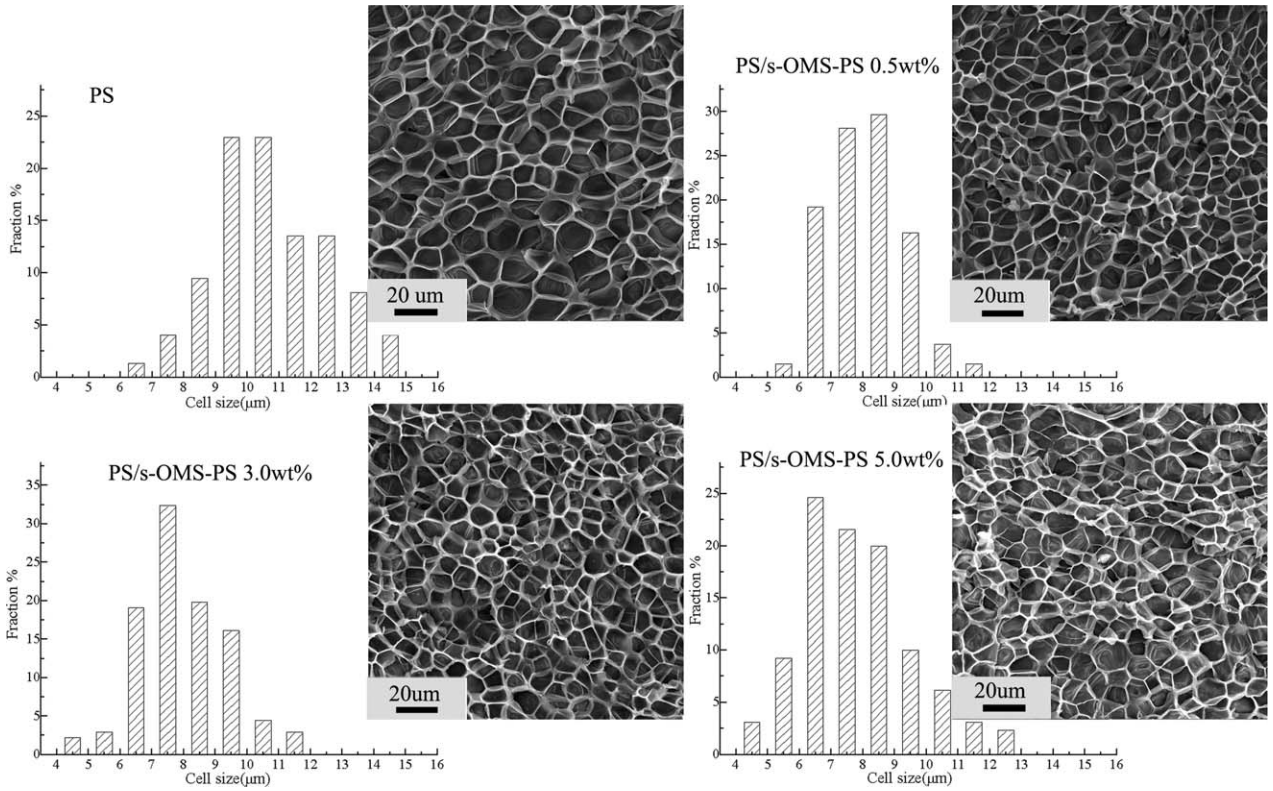

Figure 10. SEM micrographs and cell size distribution of the pure PS and composite foams (foaming conditions: 120°C and 13.8 MPa).

A batch foaming process was used to prepare PS and PS/s-OMS composite microcellular foams. In this process, the samples were quenched immediately after pressure release, through which cell coalescence could be prevented and the cell morphology could reflect the nucleation step during the foaming as much as possible. Figure 10 gives typical SEM images of the PS foam and composite foams with different contents of s-OMS. It was clear that the cell size of the PS foam decreased with the presence of s-OMS particles. By counting around 100 cells, we determined the average cell size and size distribution for these samples, as shown in Table II and Figure 10. The average cell size of the pure PS foam was around 10.7 μm, whereas the average cell size of the composite with 5.0 wt % s-OMS was around 7.8 μm, which was much smaller. The decreased cell size indicated that the heterogeneous nucleation was performed by the s-OMS particles. The cell density and the bulk density of the foam samples are shown in Table II. Similar to other composite foams with clay, carbon nanofibers, or nanotubes, the PS/s-OMS composite foams had a higher cell density compared with the pure polymer foam. The bulk densities of the composite foams were similar and even lower than that of the pure PS foam. In general, when inorganic fillers act as heterogeneous nucleation agents, they always increase the bulk density of foams. This phenomenon may be explained by the following facts. Inorganic fillers usually have a higher density than polymers. During the polymer foaming process, in addition to the heterogeneous effect, inorganic fillers also inhibit bubble growth, which decreases the cell size and increases the cell density. However, the bulk density of the foam is also increased at the same time. Herein, the bulk densities of the composite foams were almost similar or even lower than that of PS foam, meaning that the decreased cell size and increased cell density are dominantly caused by the heterogeneous nucleation effect.

Table II. Cell Sizes and Cell Densities of the PS and PS/s-OMS–PS Composite Foams

Sample	Density of the foams (g/cm^3)	Average cell size (μm)	Cell density (cell/cm^3)
PS	0.135	10.71 ± 2.08	1.35×10^9
GPPS/s-OMS–PS 0.5 wt %	0.179	8.09 ± 1.17	2.99×10^9
GPPS/s-OMS–PS 3.0 wt %	0.154	7.97 ± 1.41	3.21×10^9
GPPS/s-OMS–PS 5.0 wt %	0.122	7.80 ± 1.73	3.55×10^9

GPPS = general purpose polystyrene.
The foaming conditions were 120°C and 13.8 MPa.

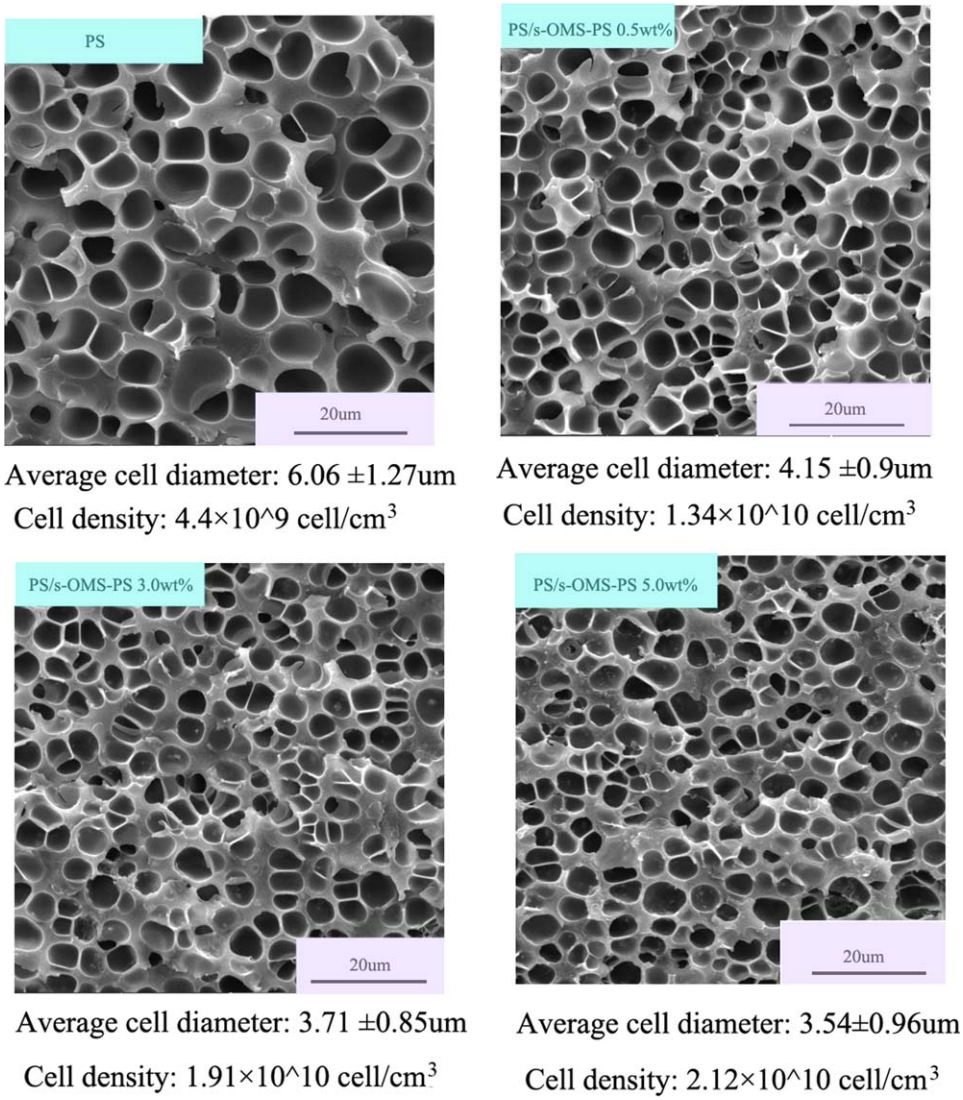

Figure 11. SEM images of the pure PS and PS/s-OMS composite foams prepared at 100°C and 13.8 MPa. [Color figure can be viewed in the online issue, which is available at wileyonlinelibrary.com.]

It is known that the foaming conditions greatly affect the nucleation during the foaming process and the final cell morphology. To elucidate the dependence of the nucleation efficiency of the s-OMS particles on the foaming variables, the PS and PS/s-OMS–PS composites were foamed at different saturation pressures and foaming temperatures. Figure 11 shows the SEM images of the PS and PS/s-OMS–PS composite foams prepared at a low foaming temperature, that is, 100°C, and the average cell diameter and cell density of these foams are also listed. The foams showed a smaller average cell diameter and a lower cell density compared to their counterparts prepared at the high foaming temperature (120°C). In the case of low saturation pressure (as shown in Figure 12), the foams had bigger average cell diameters and lower cell densities. Comparing the nucleation effects of the s-OMS particles at different foaming conditions, we observed that the nucleation effects become more significant when the foaming temperature and/or low saturation pressure were lower. For example, at 10 MPa, 5.0 wt % s-OMS particles reduced the average cell diameter from 25.2 to 10.7 μm and increased the cell density from 9.87 $\times$ 10^7 to 1.11 $\times$ 10^9 cell/cm^3.

According to classical nucleation theory,[23–25] the homogeneous and heterogeneous nucleation rates (N_{hom} and N_{het}, respectively) are expressed as follows:

$$N_{\text{hom}} = C_{\text{hom}} \exp\left(-\Delta G^*_{\text{hom}}/kT\right) \tag{4}$$

$$N_{het} = \nu_{het} C_{het} \exp\left(-\Delta G^*_{het}/kT\right) \tag{5}$$

where C_{hom} and C_{het} are the concentrations of the homogeneous and heterogeneous nucleation sites, respectively; k is the Boltzmann constant; T is the temperature; ν_{het} is the frequency factor of the gas molecules merging with the nucleus; and

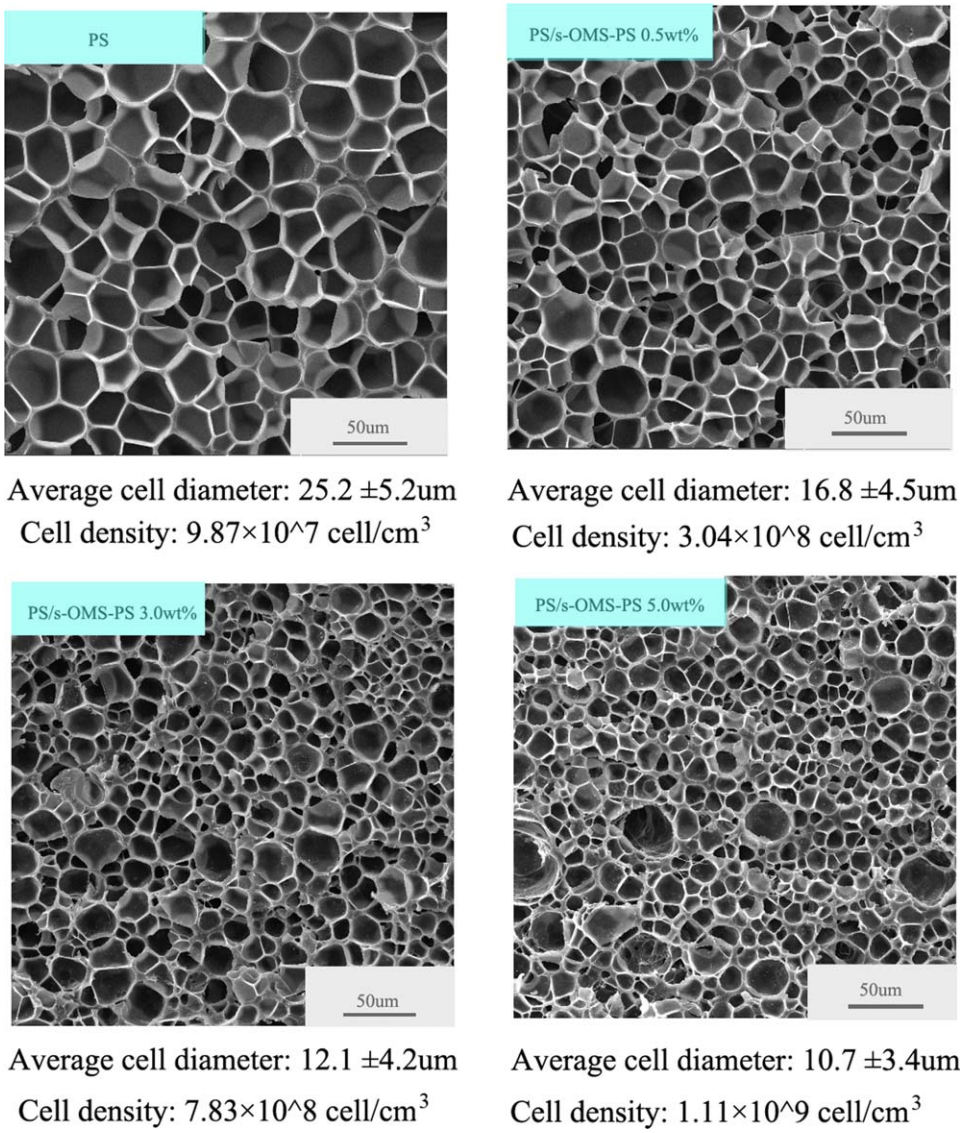

Figure 12. SEM images of the pure PS and PS/s-OMS composite foams prepared at 120°C and 10.0 MPa. [Color figure can be viewed in the online issue, which is available at wileyonlinelibrary.com.]

ΔG^*_{hom} and ΔG^*_{het} are the homogeneous Gibbs free energy and the critical Gibbs free energy needed to form a critical embryo on the nucleating sites, respectively, which are expressed as follows:

$$\Delta G^*_{het} = \frac{\Delta G^*_{\text{hom}}}{2} f(m, w) \tag{6}$$

$$\Delta G^*_{\text{hom}} = \frac{16\pi\gamma_{lv}}{3\Delta P^2} \tag{7}$$

where m is the Cosine of polymer-gas-particle contact angle, ΔG^*_{hom} is the homogeneous Gibbs free energy, which is a function of the polymer–gas surface tension (γ_{lv}) and the pressure difference (ΔP) between that inside the critical nuclei and that around the surrounding liquid. If it is assumed that the polymer is fully saturated with CO_2 and the partial molar volume of CO_2 in the polymer is zero, ΔP can be taken as the difference between the saturation pressure and the atmospheric pressure. Also, f is the reduction of critical energy due to the inclusion of nucleating agents, which is a function of the polymer–gas–particle contact angle (θ) and the relative curvature (w) of the nucleating agents surface to the critical radius of the nucleated phase.

From eqs. (6) and (7), at low temperature, both the polymer and composites have a high surface tension; this resulted in a high nucleation energy barrier. In addition, the high surface tension impeded the foam expansion, so the foams prepared at a low temperature had a relatively small average cell diameter and low cell density. In the case of low pressure, the solubility of $scCO_2$ and ΔP were lower; this resulted in the larger cell size and lower cell density. The dependence of the nucleation effect of s-OMS on the foaming conditions was caused by the difference in the free energy (ΔG^*). The free energy for heterogeneous nucleation on the surface of the s-OMS particles was lower than that for homogeneous nucleation. The difference in the free energy between heterogeneous nucleation and homogeneous nucleation increased with decreasing foaming temperature

and saturation pressure, according to eqs. (6) and (7). Therefore, the heterogeneous nucleation effect of s-OMS became more significant when the foaming temperature and saturation pressure were low. On the basis of the previous analysis, we believe that s-OMS particles could be promising heterogeneous nucleating agents for polymer foaming.

CONCLUSIONS

In summary, s-OMS particles with a high specific area were prepared. By selectively grafting the initiator, we covalently bonded the PS bushes on the surface of the s-OMS particles by surface-initiated ATRP, and the pores in the s-OMS particle were well retained and formed a core–shell structure. The modified s-OMS particles were well dispersed in the PS matrix. The porous structure and high specific area of the s-OMS particles made them good reservoirs for $scCO_2$, which compensated for the $scCO_2$ solubility loss caused by volume occupation in the composites. Upon foaming by $scCO_2$ as the blowing agent, the composite foams showed a decreased average cell size and increased cell density and, more importantly, an almost similar and even lower bulk density. The heterogeneous nucleation effect of s-OMS became more significant when the foaming temperature and saturation pressure were low. These facts indicated that the s-OMS particles could be excellent heterogeneous nucleating agents for the preparation of polymeric microcellular foams.

ACKNOWLEDGMENTS

This study was financially supported by the National Natural Science Foundation of China (contract grant numbers 50903070, 51273178, and 21274131), the Natural Science Foundation of Zhejiang Province (contract grant number LY12E03004), the Science and Technology Innovative Research Team of Zhejiang Province (contract grant number 2009R50010), and the Qianjiang Talent Project of Zhejiang Province of China (contract grant number 2010R10018).

REFERENCES

1. Lee, L. J.; Zeng, C. C.; Cao, X.; Han, X. M.; Shen, J.; Xu, G. *J. Compos. Sci. Technol.* **2005**, *65*, 2344.
2. Yeh, S. K.; Yang, J. T.; Chiou, N. R.; Daniel, T.; Lee, L. *J. Polym. Eng. Sci.* **2010**, *50*, 1577.
3. Zeng, C. C.; Zhang, C.; Wang, B.; Hossieny, N. *Polymer* **2010**, *51*, 655.
4. Juntunen, R. P.; Kumar, V.; Weller, J. E.; Bezubic, W. P. *J. Vinyl Addit. Technol.* **2000**, *6*, 93.
5. Matuana, L. M.; Park, C. B.; Balatinecz, J. *J. Cell. Polym.* **1998**, *1*, 1.
6. Jacobs, L. J. M.; Kemmere, M. F.; Keurentjes, J. T. F. *Green Chem.* **2008**, *10*, 731.
7. Fujimoto, Y.; Ray, S. S.; Okamoto, M.; Ogami, A.; Yamada, K.; Ueda, K. *Macromol. Rapid Commun.* **2003**, *24*, 457.
8. Siripurapu, S.; DeSimone, J. M.; Khan, S. A.; Spontak, R. *J. Macromolecules* **2005**, *38*, 2271.
9. Yang, J. T.; Sang, Y.; Chen, F.; Fei, Z. D.; Zhong, M. Q. *J. Supercrit. Fluids* **2012**, *62*, 197.
10. Zhu, B.; Zha, W. B.; Yang, J. T.; Zhang, C. L.; Lee, L. *J. Polymer* **2010**, *51*, 2177.
11. Taki, K.; Yanagimoto, T.; Funami, E.; Okamoto, M.; Ohshima, M. *Polym. Eng. Sci.* **2004**, *44*, 1004.
12. Yang, J. T.; Wu, M. J.; Chen, F.; Fei, Z. D.; Zhong, M. Q. *J. Supercrit. Fluids* **2011**, *56*, 201.
13. Shen, J.; Zeng, C. C.; Lee, L. *J. Polymer* **2005**, *46*, 5218.
14. Zhai, W. T.; Yu, J.; Wu, L. C.; Ma, W. M.; He, J. S. *Polymer* **2006**, *47*, 7580.
15. Marrazzo, C.; Maio, E. D.; Lannace, S. *Polym. Eng. Sci.* **2008**, *48*, 336.
16. Beck, J. S.; Vartuli, J. C.; Roth, W. J.; Leonowicz, M. E.; Kresge, C. T.; Schmitt, K. D.; Chu, C. T. W.; Olson, D. H.; Sheppard, E. W. *J. Am. Chem. Soc.* **1992**, *114*, 10834.
17. Giraldo, L. F.; López, B. L.; Pérez, L.; Urrego, S.; Sierra, L.; Mesa, M. *Macromol. Symp.* **2007**, *258*, 129.
18. Ying, J. Y.; Mehnert, C. P.; Wong, M. S. *Angew. Chem. Int. Ed.* **1999**, *38*, 56.
19. Stein, A.; Melde, B. J.; Schroden, R. C. *Adv. Mater.* **2000**, *12*, 1403.
20. Feng, Y.; Seaton, N. A. *Langmuir* **2006**, *22*, 1150.
21. Kruk, M.; Jaroniec, M.; Ryoo, R.; Kim, J. M. *Microporous Mater.* **1997**, *12*, 93.
22. Kruk, M.; Jaroniec, M. *Chem. Mater.* **1999**, *11*, 492.
23. Colton, J. S.; Suh, N. P. *Polym. Eng. Sci.* **1987**, *27*, 485.
24. Colton, J. S.; Suh, N. P. *Polym. Eng. Sci.* **1987**, *27*, 493.
25. Colton, J. S.; Suh, N. P. *Polym. Eng. Sci.* **1987**, *27*, 500.